

## Tidally Tilted Pulsations in HD 265435, a subdwarf B Star with a Close White Dwarf Companion

RAHUL JAYARAMAN <sup>1</sup>, GERALD HANDLER <sup>2</sup>, SAUL A. RAPPAPORT <sup>1</sup>, JIM FULLER <sup>3</sup>, DONALD W. KURTZ <sup>4,5</sup> AND  
GEORGE R. RICKER <sup>1</sup>

<sup>1</sup>MIT Department of Physics and MIT Kavli Institute for Astrophysics and Space Research, Cambridge, MA 02139, USA

<sup>2</sup>Nicolaus Copernicus Astronomical Center of the Polish Academy of Sciences, Bartycka 18, 00-716 Warsaw, Poland

<sup>3</sup>TAPIR, Walter Burke Institute for Theoretical Physics, Mailcode 350-17, Caltech, Pasadena, CA 91125, USA

<sup>4</sup>Centre for Space Research, Physics Department, North West University, Mahikeng 2735, South Africa

<sup>5</sup>Jeremiah Horrocks Institute, University of Central Lancashire, Preston PR1 2HE, UK

(Received February 9, 2022)

Submitted to ApJL

### ABSTRACT

Tidally tilted pulsators (TTPs) are an intriguing new class of oscillating stars in binary systems in which the pulsation axis coincides with the line of apsides, or tidal axis, of the binary. All three TTPs discovered thus far have been  $\delta$  Scuti stars. In this Letter, we report the first discovery of tidally tilted pulsations in a subdwarf B (sdB) star. HD 265435 is an sdB–white dwarf binary with a 1.65-hr period that has been identified and characterized as the nearest potential Type Ia supernova progenitor. Using TESS 20-s cadence data from Sectors 44 and 45, we show that the pulsation axis of the sdB star has been tidally tilted into the orbital plane and aligned with the tidal axis of the binary. We identify 31 independent pulsation frequencies, each with between 1 and 7 sidebands separated by the orbital frequency ( $\nu_{\text{orb}}$ ), or multiples thereof. Using the observed amplitude and phase variability due to tidal tilting, we assign  $\ell$  and  $m$  values to most of the observed oscillation modes, and use these mode identifications for preliminary asteroseismic constraints. Our work significantly expands our understanding of TTPs, because we now know that (i) they can be found in stars other than  $\delta$  Scuti pulsators, especially highly-evolved stars that have lost their H-rich envelopes, and (ii) tidally tilted pulsations can be used to probe the interiors of stars in very tight binaries.

### 1. INTRODUCTION

#### 1.1. Tidally Tilted Pulsators

Tidally tilted pulsators (TTPs) are a class of stars in which the pulsation axis of an oscillating star in a close binary system coincides with the line of apsides of the binary, i.e., the tidal axis, rather than the star’s spin axis. Such stars were first discovered using photometric data from the Transiting Exoplanet Survey Satellite mission (TESS; Ricker et al. 2015). Three TTPs have been conclusively identified so far, all from TESS data: HD 74423 (Handler et al. 2020), CO Cam (Kurtz et al. 2020), and TIC 63328020 (Rappaport et al. 2021). Other potential tidally tilted pulsators include U Gru (Bowman et al. 2019) and V456 Cyg (Van Reeth et al. 2022), but fur-

ther work is required to characterize these stars’ tidally tilted nature. For detailed descriptions and analyses of these intriguing objects, we direct the reader to the recent reviews of Handler et al. (2022) and Fuller et al. (2020), and the references therein.

The immediately important property of TTPs is that for binary systems with orbital inclination angle  $i \sim 90^\circ$ , the observer can view the star through a range of latitudinal angles with respect to the pulsation axis, from  $0^\circ$  to  $360^\circ$ . In turn, this changing view direction with orbital phase enables the observer to better identify the pulsation modes being studied. This does not happen in most single stars or ordinary pulsators in binaries; in these, the observer’s view direction remains constant with respect to the pulsation axis. The one exception is encountered in roAp stars (see, e.g., Kurtz et al. 1992), where the pulsation axis has been tilted with respect to the spin axis by the star’s magnetic field.

58 The three TTPs mentioned previously are all  $\delta$  Scuti  
 59 stars. This naturally raises the question as to whether  
 60 tidally tilted pulsations can be observed in other types of  
 61 pulsating stars, such as those that are no longer on the  
 62 main sequence, or if such pulsations are dependent on  
 63 some inherent property of  $\delta$  Scuti stars. Theory suggests  
 64 that the latter is unlikely, as the modeling of TTPs in  
 65 Fuller et al. (2020) does not in any way rule out tidally  
 66 tilted pulsations in other kinds of stars. Searches are  
 67 underway in TESS data to detect these unique systems.

### 68 1.2. *sdB Asteroseismology with TESS*

69 Subdwarf B (sdB) stars are core helium-burning stars  
 70 with very thin hydrogen envelopes; such objects have  
 71 been found to exhibit significant chemical peculiarities.  
 72 These stars are commonly thought to be the stripped  
 73 cores of red giants, and lie on the Extreme Horizontal  
 74 Branch of the Hertzsprung-Russell (H-R) Diagram, with  
 75  $T_{\text{eff}}$  anywhere between 20 000 K and 45 000 K. For a de-  
 76 tailed description of sdB stars and their properties, we  
 77 point the reader to the review of Heber (2016).

78 Many sdB stars are known to pulsate; the first pulsat-  
 79 ing sdB star was discovered by Kilkenny et al. (1997).  
 80 Since then, over 100 such stars have been discovered  
 81 (Holdsworth et al. 2017). Some sdBs pulsate with rapid  
 82 p mode oscillations, having periods on the order of a few  
 83 minutes; others pulsate with slower g mode oscillations,  
 84 having periods that are on the order of a few hours; and  
 85 a few stars show a combination of these two. TESS has  
 86 proven key in the study of rapidly pulsating sdBs, due  
 87 to the 20-s cadence data mode introduced at the start  
 88 of the Extended Mission in 2020 July. This ultra-short-  
 89 cadence mode can probe frequencies up to a Nyquist  
 90 limit of  $2160 \text{ d}^{-1}$ , corresponding to periods as short as  
 91 40 s. Consequently, TESS has been at the vanguard of  
 92 sdB asteroseismology (see, e.g., Section 6 of Lynas-Gray  
 93 2021, and references therein).

### 94 1.3. *HD 265435*

95 HD 265435 (TIC 68495594) is an sdB–white dwarf bi-  
 96 nary that was studied extensively by Pelisoli et al. (2021)  
 97 and identified as the closest potential Type Ia super-  
 98 nova progenitor, with a possible thermonuclear detona-  
 99 tion occurring in approximately 70 Myr. Pelisoli et al.  
 100 focused primarily on characterizing the properties of the  
 101 system, including the stellar parameters, the radial ve-  
 102 locity of the subdwarf, and the nature of the companion  
 103 – which they found to be a white dwarf.

104 Pelisoli et al. reported that the subdwarf component  
 105 of HD 265345 is a pulsator with a rich mode spectrum  
 106 but noted, however, that the Nyquist limit of the 2-min  
 107 cadence data available to them ( $360 \text{ d}^{-1}$ , corresponding

108 to a period of 4 min) prevented them from conducting  
 109 a full asteroseismic analysis of the subdwarf component  
 110 of the binary. This problem is overcome with the latest  
 111 release of 20-s cadence data from TESS sectors 44 and  
 112 45, which show an incredibly rich pulsation spectrum  
 113 for the sdB star. In this Letter, we use all the available  
 114 ultra-short-cadence data for this star to characterize its  
 115 pulsations and study their tidally tilted nature.

## 116 2. OBSERVATIONS

### 117 2.1. *TESS Data*

118 HD 265435 was observed at 2-min cadence in Sector  
 119 20 (from 2019 December 24 to 2020 January 21), at  
 120 20-s cadence in Sectors 44 and 45 (from 2021 October  
 121 12 to 2021 December 2), and at 10-min cadence in the  
 122 full-frame images during Sector 47 (from 2021 Decem-  
 123 ber 30 to 2022 January 28). The shorter-cadence data  
 124 are available in both SAP (simple aperture photometry)  
 125 and PDCSAP (presearch data conditioning SAP) forms.  
 126 Data processing was done using the SPOC pipeline at  
 127 the NASA Ames Research Center (Jenkins et al. 2016).  
 128 We used the 20-s SAP data from both Sectors 44 and  
 129 45 to investigate the frequencies of interest. These data  
 130 span 50.35 d, and comprise 190 194 data points, after  
 131 clipping to remove outliers – such as those arising from  
 132 scattered light or cosmic ray strikes on the CCD.<sup>1</sup>

133 Every sector, we manually review the Fourier spec-  
 134 tra of all the 20-s targets observed by TESS to search  
 135 for particularly high-frequency pulsations in the data.  
 136 HD 265435 was flagged for further follow-up due to the  
 137 combination of: (i) an obvious set of orbital harmon-  
 138 ics from a binary light curve (see Figure 1), with the  
 139 second harmonic being the strongest due to ellipsoidal  
 140 light variations, and (ii) an incredibly rich set of pul-  
 141 sations between frequencies of 150 and  $400 \text{ d}^{-1}$  (see  
 142 Figure 2). The presence of both of these features is  
 143 a rather unusual occurrence in an sdB star. Moreover,  
 144 the two strongest peaks in the pulsation spectrum ap-  
 145 pear to be spaced by exactly twice the orbital frequency  
 146 ( $\nu_{\text{orb}}$ ), which prompted us to investigate further. It then  
 147 became apparent that there are numerous peaks with  
 148 frequency spacings equal to multiples of  $\nu_{\text{orb}}$ ; these were  
 149 noticed by Pelisoli et al. and interpreted as rotationally  
 150 split modes in the synchronously rotating sdB star.

## 151 3. PULSATONAL FREQUENCY ANALYSIS

152 A detailed frequency analysis of the TESS data was  
 153 performed with the PERIOD04 software (Lenz & Breger  
 154 2005). This package produces amplitude spectra by

<sup>1</sup> Data release notes for every TESS sector are available at this  
 link: [https://archive.stsci.edu/tess/tess\\_drn.html](https://archive.stsci.edu/tess/tess_drn.html).

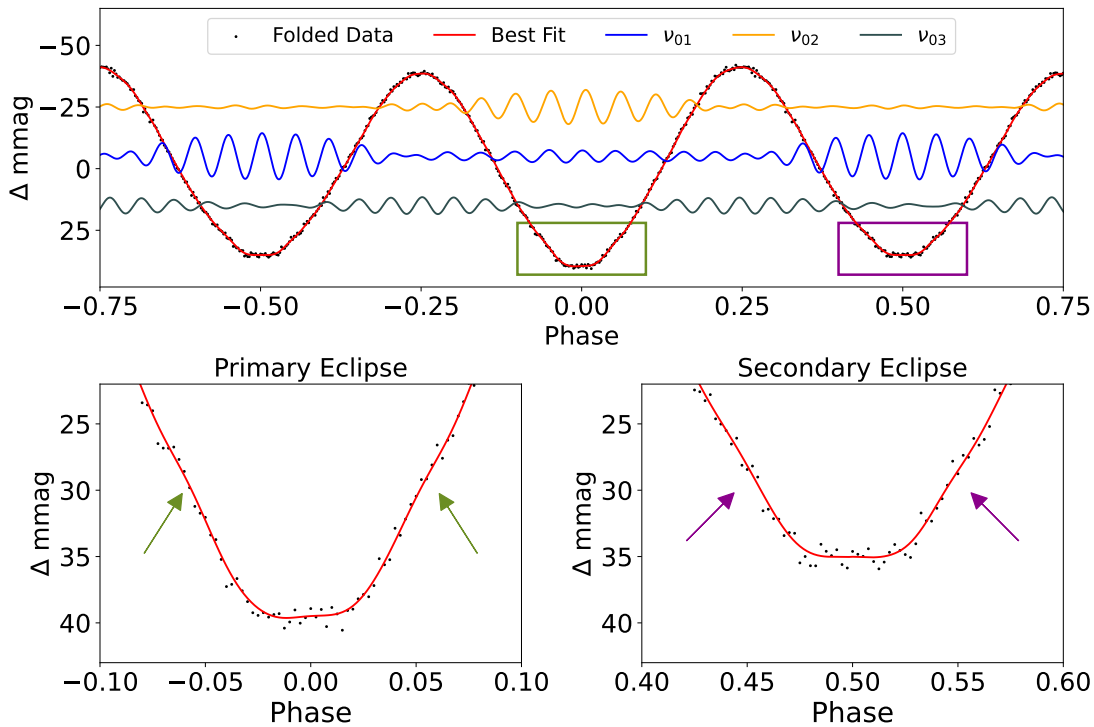


**Figure 1.** A phase-folded light curve with zooms on possible primary and secondary eclipses. The black points correspond to the actual data, while the red light curve represents a best-fit curve derived from the frequencies removed when prewhitening the orbital harmonics. The boxes in the top panel mark the locations of the zoomed-in plots, where arrows identify the start and end of potential eclipses. The best-fit light curve was smoothed with a Savitsky-Golay filter (Savitzky & Golay 1964) to remove any short-term variability not arising from the orbital modulations. The blue, yellow, and gray curves in the top panel are reconstructions of the multiplets  $\nu_{01}$ ,  $\nu_{02}$  and  $\nu_{03}$ , with amplitudes equal to their actual values but offset vertically for clarity.

155 Fourier analysis, and can also perform multi-frequency  
 156 least-squares sine-wave fitting. It also includes advanced  
 157 options such as the calculation of optimal light-curve fits  
 158 for multiperiodic signals including harmonic, combina-  
 159 tion, and equally spaced frequencies. The optimal sine-  
 160 wave fits to the light curve were subtracted from the  
 161 data, and the residuals then examined for further peri-  
 162 odicities. To decide whether or not to include a given  
 163 signal in the overall frequency solution, we required its  
 164 amplitude to exceed the local noise level by a factor  
 165 of 4.5 (i.e.,  $S/N > 4.5$ ). This criterion was relaxed to  
 166  $S/N > 3.5$  in the case of signals at predicted frequencies,  
 167 i.e., multiplet members or combination frequencies.

168 We first found the orbital ephemeris of HD 265435. In  
 169 order to calculate this to the highest possible accuracy,  
 170 we merged the TESS data sets from Sectors 20, 44, and  
 171 45 into 6-min bins to suppress the pulsational variations.  
 172 An initial check showed that the amplitude of the or-  
 173 bital variation was  $\sim 10\%$  smaller in Sector 20 compared  
 174 to Sector 44, and  $\sim 6\%$  smaller in Sector 45 compared to  
 175 Sector 44. This is certainly an effect of imperfect cor-  
 176 rection for the flux of a neighboring star falling into the  
 177 photometric aperture of our target (for details, see the  
 178 Methods section of Pelisoli et al.). Thus, we scaled the

179 amplitudes of the Sector 20 and 45 data to match that  
 180 of the Sector 44 data and determined the ephemeris for  
 181 the times of the deeper ellipsoidal light minima  $T_I$  of the  
 182 system, corresponding to the orbital phase where the L1  
 183 point is directed towards the observer:

$$184 \quad T_I = 2459500.32517(9) + 0.068818543(2)E \text{ (BJD)},$$

185 where  $E$  is the epoch, i.e., the number of orbital cycles  
 186 elapsed. We also note that the orbital ephemeris derived  
 187 by Pelisoli et al. contains a typographical error (their  
 188 BJD<sub>0</sub> should actually be 2458909.689955(3)); in con-  
 189 trast to our  $T_I$ , theirs corresponds to an orbital phase  
 190 where the L2 point is directed towards the observer.

191 Figure 1 shows the phase-folded, binned light curve of  
 192 this system. To calculate the best-fit light curve, we used  
 193 the amplitudes and phases of the frequencies of the first  
 194 100 orbital harmonics. We highlight the flat-bottomed  
 195 regions near the minima of the ellipsoidal light varia-  
 196 tions, which hint at the possibility of a grazing eclipse.  
 197 We note that the presence of an eclipse, if our interpre-  
 198 tation of this feature is correct, would imply a larger  
 199 inclination angle than found by Pelisoli et al. They es-  
 200 timated  $i = 60^\circ - 76^\circ$ , whereas eclipses would require

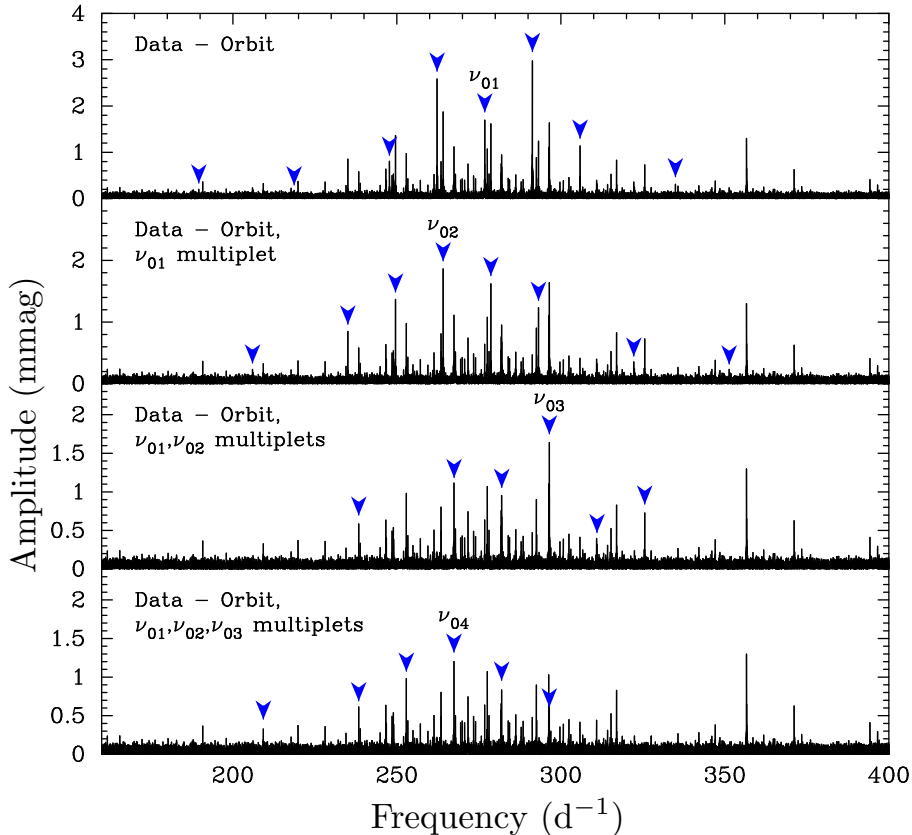


**Figure 2.** The Fourier amplitude spectrum in the range of the pulsation frequencies, with successive plots (going row-by-row) that highlight the sequential prewhitening of frequency multiplets. The central components of these multiplets are indicated with their identifiers according to Table 1, and the blue arrows point at all of the multiplet components.

201 inclinations of roughly  $80^\circ - 85^\circ$ . This would, in turn,  
 202 somewhat lower the mass determined for the sdB star.

### 203 3.1. The pulsation frequencies

204 We subtracted the zeropoint in time ( $T_0$ , as deter-  
 205 mined above) from the time series, fitted the orbital vari-  
 206 ation to the data using 100 orbital harmonics and then  
 207 pursued our frequency analysis with PERIOD04. The  
 208 orbital and the pulsation frequency fit were performed  
 209 simultaneously for the highest possible accuracy and reli-  
 210 ability. The top panel in Figure 2 shows the resultant  
 211 discrete Fourier transform (see, e.g., Kurtz 1985) cover-  
 212 ing the frequency range from 160 to  $400 \text{ d}^{-1}$ . The blue  
 213 arrows mark the most prominent frequency and its side-  
 214 bands, which are produced by the tidal tilting of the pul-  
 215 sation axis and spaced by the orbital frequency. These  
 216 groups are called “multiplets.” The sequence of three  
 217 lower panels in Figure 2 shows the sequential prewhiten-  
 218 ing (described below) of several pulsation frequency mul-  
 219 tiplets all split by the orbital frequency. This plot illus-  
 220 trates the complexity of the rich pulsation spectrum.

221 For each multiplet, we adopt the frequency of the cen-  
 222 tral peak and force the other multiplet frequencies to be  
 223 separated from it by integer multiples of the orbital fre-  
 224 quency. We then do a simultaneous least squares fit for  
 225 all the amplitudes and phases of that multiplet. The  
 226 entire multiplet is then subtracted from the data. This  
 227 sequential prewhitening process resulted in 31 independ-  
 228 ent mode frequencies, 90 multiplet components split  
 229 by integer multiples of the orbital frequency, and seven  
 230 combination frequencies. The complete frequency solu-  
 231 tion after simultaneous optimization of all frequencies,  
 232 amplitudes, and phases for the pulsations is in Table 1.

233 A convenient way of visualizing multiplets is via an  
 234 échelle diagram, where the frequency of a pulsation is  
 235 plotted on the vertical axis, and the échelle “phase” (the  
 236 pulsation frequency modulo the orbital frequency, nor-  
 237 malized to the orbital frequency) is displayed on the  
 238 horizontal axis. The échelle diagram for HD 265435 is  
 239 presented in Figure 3. Each vertical string of points rep-  
 240 resents a multiplet, i.e., an independent pulsation fre-  
 241 quency split by multiples of the orbital frequency.

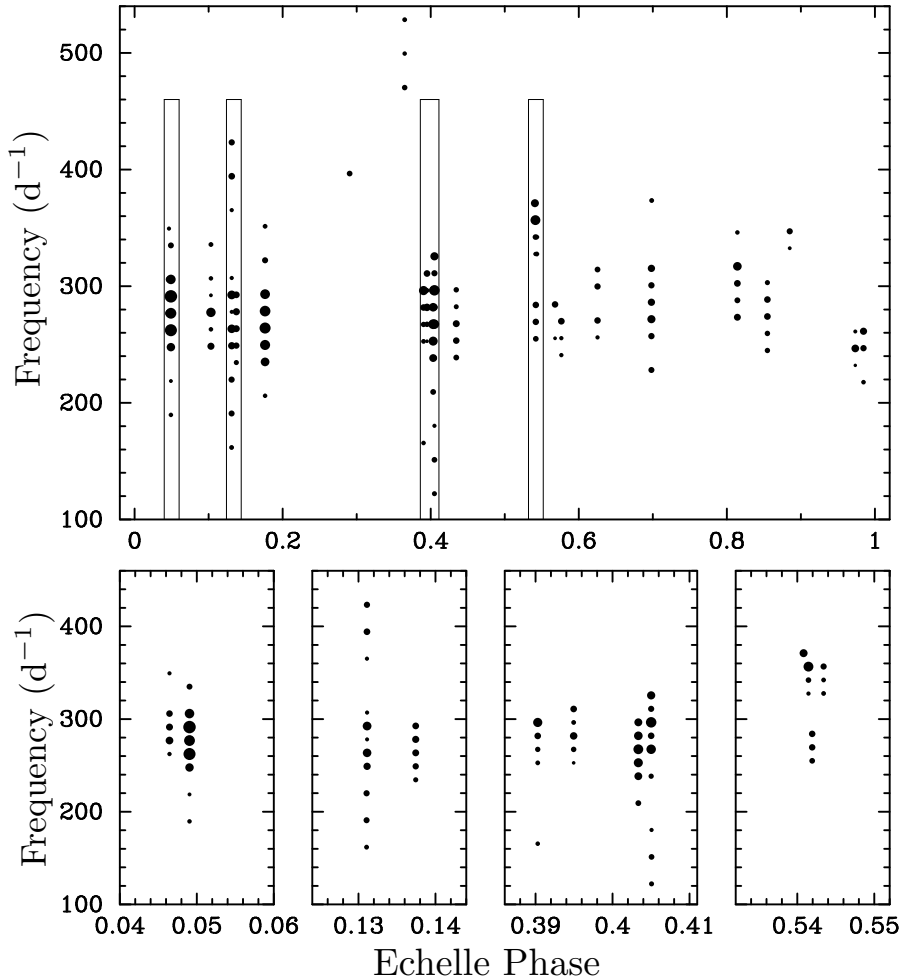


**Figure 3.** Échelle diagram of the pulsation frequencies with respect to the orbital frequency. The size of the filled circles is proportional to the amplitude of that particular constituent of the multiplet. The upper panel shows the full range of frequencies; the lower panels are zooms into regions that are not resolved in the upper panel but contain multiple sequences of frequencies. These regions are denoted with rectangles in the upper panel. The x-axis label "Echelle Phase" is defined as the pulsation frequency modulo the orbital frequency, normalized to the orbital frequency.

As noted previously, Pelisoli et al. ascribed the pulsational frequencies of the subdwarf that are visible in the 2-min data to rotationally split multiplets. We argue in the following paragraphs that this is not the case. Rather, the sidelobes of any given pulsation frequency in this star describe the amplitude and phase modulation of that particular mode as a consequence of the time-varying latitudinal viewing angle (with respect to the pulsation axis) over one full orbital cycle.

Rotationally split multiplets have frequencies

$$\nu_{n,\ell,m} = \nu_{n,\ell} + m(1 - C_{n,\ell})\Omega, \quad (1)$$

where  $n, \ell, m$  are the radial order, degree, and azimuthal order, respectively;  $C_{n,\ell}$  is the "Ledoux constant"; and  $\Omega$  is the rotation frequency. For models of pulsating sdB stars, Charpinet et al. (2000) find  $C_{n,\ell} \gtrsim 0.02$ .

For HD 265435, rotationally split modes are ruled out, as that would require  $C_{n,\ell}$  to precisely approach 0 to within the observational error, which is on the order of one part in  $10^5$ . Furthermore, nearly all of the modes reach pulsation amplitude maximum at the time the tidal axis crosses the line of sight, or  $90^\circ$  from that, as expected for oblique pulsation - for a visual representation, see Figure 4. This behavior is not expected for a rotationally split mode, as the location of the pulsation amplitude maximum in that particular case would drift with orbital phase on a timescale set by  $C_{n,\ell}$ .

Finally, some of the highest amplitude multiplets contain components out to  $4\nu_{\text{orb}}$  and  $6\nu_{\text{orb}}$ , suggesting that these would correspond to high values of  $\ell$  in the rotationally split multiplet interpretation. Such high degree modes have very low visibility due to geometrical cancel-

lution (Dziembowski 1977) and are therefore not a plausible explanation for the modes observed in HD 265435. As a result, we are able to conclusively rule out the rotational splitting explanation and can conclude that HD 265435 is a tidally tilted pulsator.

Now that we have established that the frequency multiplets are spaced by exactly the orbital frequency, with the central frequency being the actual pulsation mode frequency, we note that there are, in addition, two other effects that contribute to the orbital sidelobes.

The first arises because of frequency modulation caused by the Doppler shift of the pulsation frequency with orbital motion (Shibahashi & Kurtz 2012). That effect contributes up to a few tenths of a mmag to the first orbital sidelobes of the frequency multiplets, but with phases such that there is no contribution of this effect to the measured pulsation amplitude at any orbital phase. In other terms, this effect does not contribute at all to the pulsation amplitudes plotted in Figure 4 and modeled in Section 4, since Doppler shifts affect only frequency and not amplitude. When describing pulsations using sinusoids, the frequency variability is equivalent to phase variations; thus, this effect does contribute to the phase variations in Figure 4 but is utterly undetectable. The semi-major axis of the orbit is only  $0.83 R_{\odot}$  as per Pelisoli et al. (2021), and the orbital motion of the sdB star has a radius from the barycenter of only  $0.51 R_{\odot}$ , which is just 1.2 light-seconds. With pulsation periods on the order of 250 s, the phase variation caused by the orbital motion ( $\sim 0.03$  rad) is inconsequential.

The second additional contribution to the orbital sidelobes of the frequency multiplets comes from changes in the background light due to ellipsoidal light variations. Those are  $\sim 75$  mmag peak-to-peak; consequently, for a constant pulsation amplitude, they cause an apparent modulation of the pulsation amplitude by 0.075. That will affect the sidelobes' amplitudes, but only to the amount that the pulsation amplitude modulates by – for

example, 0.75 mmag peak-to-peak for a 10 mmag pulsation. That is also not the source of the orbital amplitude variations seen in Figure 4 and in the models that we can now ascribe to tidally tilted pulsations.

### 3.2. Reconstructing the Amplitude-Phase Curve of a Multiplet

For each multiplet, we have a collection of amplitudes  $\{a_n\}$  and phases  $\{\phi_n\}$ . The amplitudes and phases of the constituent peaks in the multiplet were found as described in Section 3.1. All the information about a given multiplet that is available from the data set is also wholly contained in the set of  $a_n$ 's and  $\phi_n$ 's.

The time dependence of the pulsation in a given multiplet  $\mathcal{M}(t)$  can be written as follows:

$$\mathcal{M}(t) = \sum_{n=-\min}^{n=\max} a_n \cos(\omega_{\text{osc}}t + n\omega_{\text{orb}}t + \phi_n), \quad (2)$$

where  $t$  is measured from the time where phase zero has been defined,  $\omega_{\text{osc}}$  and  $\omega_{\text{orb}}$  are the oscillation and orbital angular frequencies, respectively, and  $n = 0$  defines the best estimate of the central element of the multiplet.

We can expand the cosine function and remove the terms dependent on  $\omega_{\text{osc}}$  from the summation to find:

$$\begin{aligned} \mathcal{M}(t) = \cos(\omega_{\text{osc}}t) & \sum_{n=-\min}^{n=\max} a_n \cos(n\omega_{\text{orb}}t + \phi_n) - \\ & \sin(\omega_{\text{osc}}t) \sum_{n=-\min}^{n=\max} a_n \sin(n\omega_{\text{orb}}t + \phi_n) \end{aligned} \quad (3)$$

We rewrite this expression with basic trigonometric identities in the following suggestive form, where we recast  $\omega_{\text{orb}}$  in terms of orbital phase  $\Phi_{\text{orb}}$  as  $\omega_{\text{orb}}t = \Phi_{\text{orb}}$ :

$$\mathcal{M}(t) = \mathcal{A}_{\text{osc}}(t, \Phi_{\text{orb}}, \{a_n\}, \{\phi_n\}) \cos[\omega_{\text{osc}}t + \Phi_{\text{osc}}(t, \Phi_{\text{orb}}, \{a_n\}, \{\phi_n\})] \quad (4)$$

Here,  $\mathcal{A}_{\text{osc}}$  and  $\Phi_{\text{osc}}$  are defined as:

$$\mathcal{A}_{\text{osc}} \equiv \sqrt{\left( \sum_{n=-\min}^{n=\max} a_n \cos(n\Phi_{\text{orb}} + \phi_n) \right)^2 + \left( \sum_{n=-\min}^{n=\max} a_n \sin(n\Phi_{\text{orb}} + \phi_n) \right)^2} \quad (5)$$

$$\Phi_{\text{osc}} \equiv \text{ArcTan2} \left\{ \left( \sum_{n=-\min}^{n=\max} a_n \sin(n\Phi_{\text{orb}} + \phi_n) \right), \left( \sum_{n=-\min}^{n=\max} a_n \cos(n\Phi_{\text{orb}} + \phi_n) \right) \right\}, \quad (6)$$

$\mathcal{A}_{\text{osc}}$  and  $\Phi_{\text{osc}}$  are the amplitude and phase of the multiplet and their dependence on  $\Phi_{\text{orb}}$ , the orbital phase.

Note that the amplitude and phase of the multiplet do not depend explicitly on the frequency of either the mul-

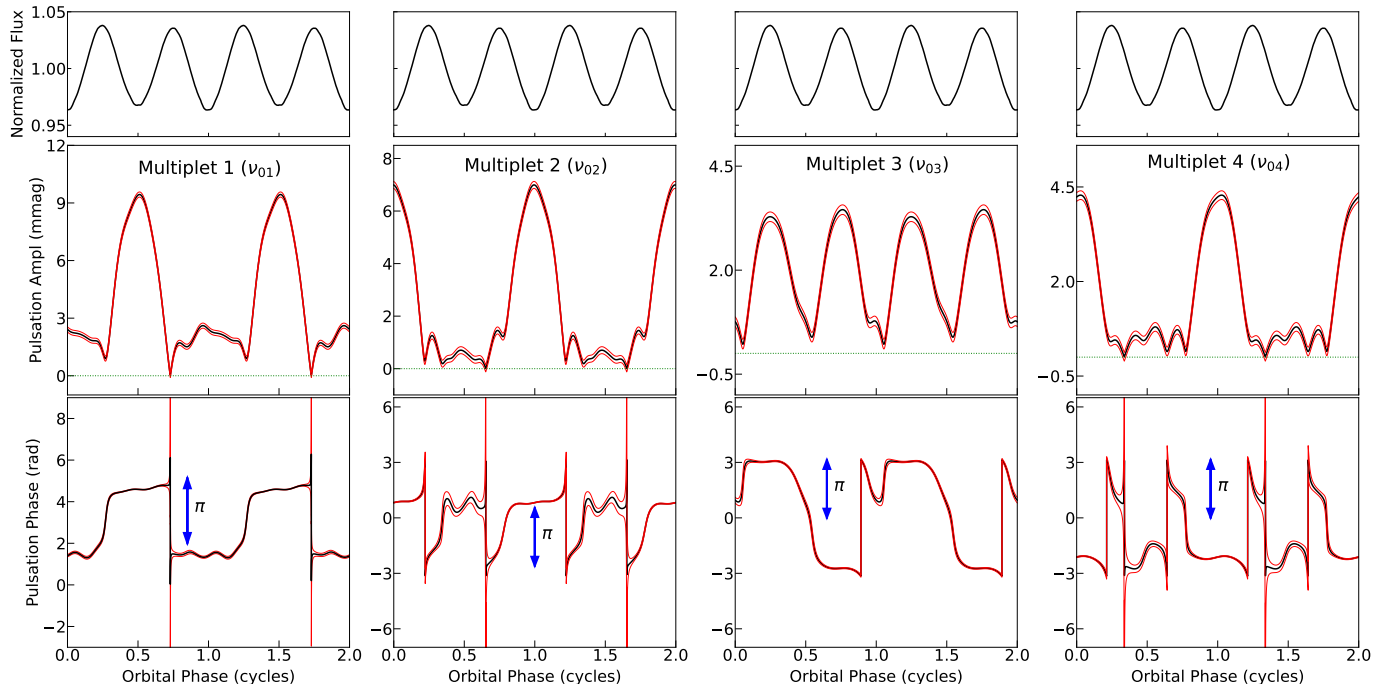


**Figure 4.** Pulsation phase and amplitudes for multiplets centered on the frequencies  $\nu_{01}$ ,  $\nu_{02}$ ,  $\nu_{03}$ , and  $\nu_{04}$ ; these were calculated from the analytical expressions in Equations 5 and 6. Red lines represent formal  $1\text{-}\sigma$  uncertainties on the values of amplitude and phase; following Montgomery & O’Donoghue (1999), these were calculated as  $\sigma_{\text{ampl}} = \sqrt{2m/n}\sigma_a$ , where the observational rms scatter per single data point  $\sigma_a = 14.61$  mmag,  $n$  is the number of data points (190,194), and  $m$  is the number of detectable peaks in the mode (6-8). In turn,  $\sigma_{\text{ph}} = \sigma_{\text{ampl}}/a(\Phi_{\text{orb}})$ , where  $a(\Phi_{\text{orb}})$  is the amplitude at a given orbital phase  $\Phi_{\text{orb}}$ . Blue arrows on the phase plots, denoting a length of  $\pi$ , provide a sense of scale. The dotted green lines in the second row of plots denote a pulsation amplitude of zero, i.e., locations where the pulsation phase cannot be meaningfully calculated.

348 triplet or the orbit. We have also used the ArcTan2 function to ensure that the phase of the pulsation is located in the correct Cartesian quadrant.  
349  
350

### 351 3.3. The Multiplet Amplitude and Phase Diagrams

352 We utilize the expression for the multiplet amplitude as a function of orbital phase from Equation (5) and for the multiplet phase from Equation (6) to analytically reconstruct how the multiplet pulsation varies in amplitude and phase around the orbit. Figure 4 contains these amplitude-phase plots for the four most prominent multiplets. Multiplets  $\nu_{01}$  and  $\nu_{02}$  have maximum amplitudes when the observer is viewing the L2 and L1 points, respectively. These are  $m = 0$  modes, in which the pulsation amplitudes are highly suppressed at one end or the other of the elongated (i.e., tidally distorted) sdB star. There are phase shifts of  $\pi$  at the times of ellipsoidal maxima, as expected for such a mode. Multiplet  $\nu_{03}$  has its maxima at each of the ellipsoidal maxima, and is thus inferred to be an  $|m| = 2$  mode (see Sect. 4), with no  $\pi$  phase jumps. Multiplet  $\nu_{04}$  is very similar in behavior to that of multiplet  $\nu_{02}$ . Note that the phases after the apparent discontinuity in these two multiplets’ plots are identical (phases  $\pi$  and  $-\pi$  are identical), so this “jump” does not represent anything meaningful, un-

372 like the  $\pi$  phase shift (discussed previously) that is observed in the phases of multiplets  $\nu_{01}$  and  $\nu_{02}$ .  
373

### 374 4. ASTEROSEISMIC MODELING

375 To model the tidally tilted pulsations of HD 265435, we follow the same procedure described in Fuller et al. (2020). We (i) construct a stellar model, (ii) compute non-adiabatic pulsation modes for the spherical star, (iii) calculate tidal coupling coefficients and solve for the new set of tidally coupled modes, and finally (iv) predict the amplitude and phase variation of the calculated modes as a function of orbital phase.  
380  
381  
382

383 Our sdB models are made with the MESA stellar evolution code (Paxton et al. 2011, 2013, 2015, 2018, 2019). First we evolve a  $3.2 M_{\odot}$  star up the red giant branch, and then strip the hydrogen envelope until only the  $0.5 M_{\odot}$  core remains, which still contains  $\sim 0.02 M_{\odot}$  of hydrogen. We then enable atomic diffusion (but not radiative levitation) and evolve the star through the core helium-burning phase until it expands slightly to  $R \simeq 0.21 R_{\odot}$  and  $T_{\text{eff}} \simeq 34,000$  K. At this point, we compute oscillation modes with GYRE (Townsend & Teitler 2013; Goldstein & Townsend 2020), including modes with  $0 \leq \ell \leq 10$  and frequencies ranging from  $2 f_{\text{dyn}} \lesssim f \lesssim 8 f_{\text{dyn}}$ . Our stellar model has  
395

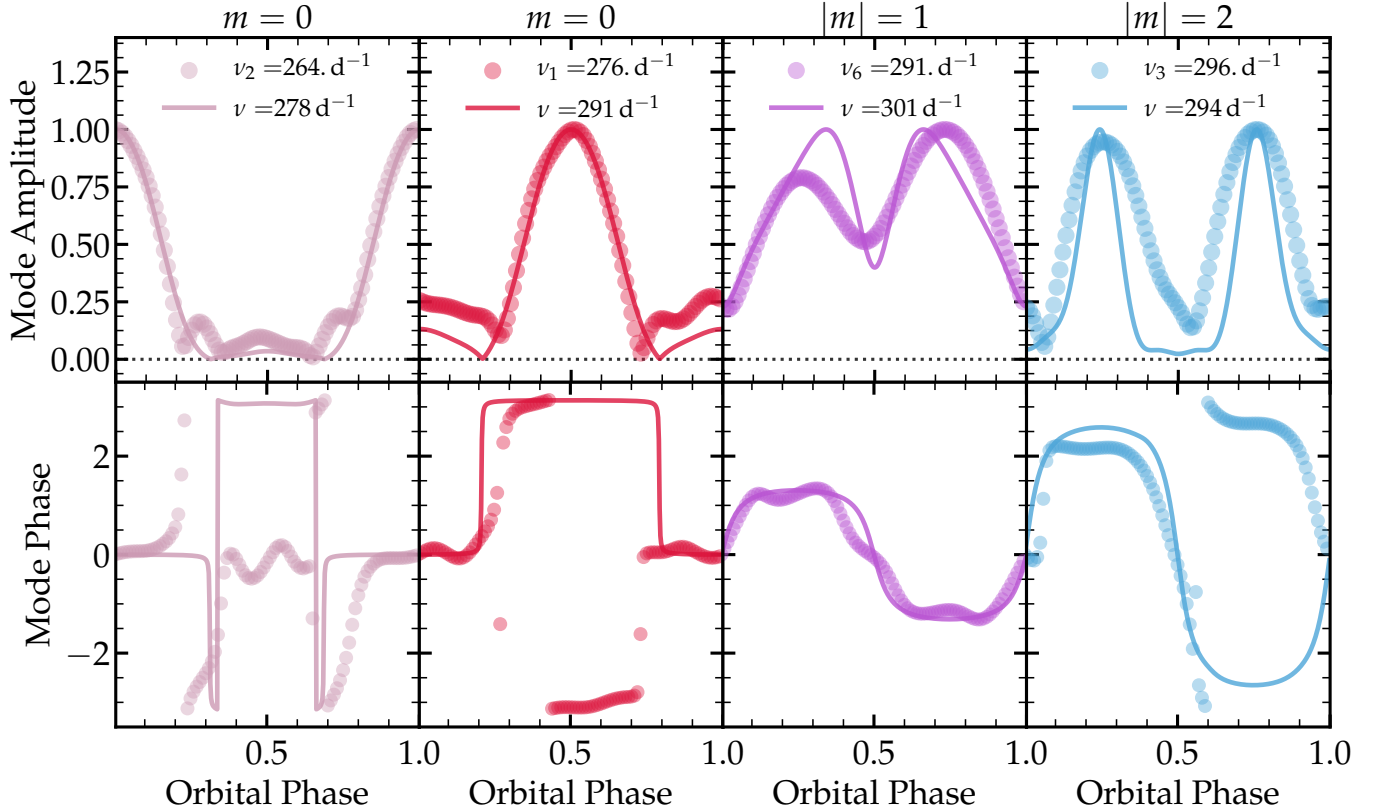


**Figure 5.** Comparison between observed modes (circles) and modeled modes (lines) for a subset of the pulsations of TIC 68495594. Top panels compare amplitudes (normalized to maximum), while bottom panels compare mode phases, as a function of orbital phase. Columns are labeled by the  $m$  value likely to correspond to the observed mode. The modeled modes are selected by choosing modes with the appropriate value of  $m$ , frequencies near  $\sim 290 \text{ d}^{-1}$ , and with luminosity fluctuations larger than surrounding modes (such that the mode is not strongly trapped in the core, and is not dominated by high- $\ell$  components). Note that phase  $-\pi$  and  $\pi$  are identical, so the match with the phases of the  $\nu_1$  and  $\nu_3$  modes is better than it appears.

396  $f_{\text{dyn}} = \omega_{\text{dyn}}/(2\pi) \simeq 65 \text{ d}^{-1}$ , so this frequency range cor-  
397 responds roughly to the observed range of frequencies  
398 shown in Figure 2.

399 In our stellar model, the frequency range where most  
400 of the observed modes cluster ( $260\text{--}300 \text{ d}^{-1}$ ) corresponds  
401 to the first overtone ( $n = 2$ )  $\ell = 0$  and  $\ell = 1$  acoustic  
402 modes. For slightly more massive or compact models,  
403 the observed frequencies would correspond to the fun-  
404 damental ( $n = 1$ )  $\ell = 0$  and  $\ell = 1$  acoustic modes. Our  
405 stellar model has just finished helium burning, so it also  
406 contains a radiative core that allows for a fairly dense  
407 spectrum of g modes at these frequencies. For models  
408 with a convective helium-burning core, the observed fre-  
409 quencies correspond to low-order gravity modes ( $n_g \sim 1$   
410 for  $\ell = 1$ ) trapped just outside the convective core. In  
411 either case, the observed modes with non-radial compo-  
412 nents may be mixed modes.

413 Following Fuller et al., we compute the eigenfunctions  
414 of modes aligned with the tidal axis for azimuthal num-  
415 bers of  $m = 0$ ,  $m = -1$ , and  $m = -2$ . By integrating  
416 the surface flux perturbations of these modes over the

417 observable hemisphere, we then calculate the mode am-  
418 plitudes and phases over the orbital cycle. We assume  
419 an orbital inclination of  $i = 75^\circ$ . Figure 5 shows predic-  
420 tions for the amplitude and phase variation of several  
421 example modes during the orbital cycle, in comparison  
422 to a few observed modes. We find many different types  
423 of tidally tilted and tidally trapped pulsations.

424 For  $m = 0$  modes, we find examples of modes that  
425 are strongly trapped on the  $L_1$  side of the star (simi-  
426 lar to the observed mode  $\nu_{02}$ , shown in the first panel  
427 of Figure 5), whose amplitudes peak near orbital phase  
428 0. We also find modes that are strongly trapped on the  
429  $L_2$  side (similar to the observed mode  $\nu_{01}$ , shown in the  
430 second panel Figure 5), whose amplitudes peak near or-  
431 bital phase 0.5. There are other axisymmetric modes  
432 that are not trapped in either hemisphere (similar to  
433 the observed mode  $\nu_{07}$ ) whose amplitudes peak at both  
434 orbital phase 0 and 0.5. Axisymmetric modes typically  
435 have phase shifts of  $\sim 0$  or  $\sim \pi$  over the orbit depend-  
436 ing on whether their eigenfunctions are dominated by  $\ell = 0$   
437 or  $\ell = 2$  (like  $\nu_{02}$ ) or  $\ell = 1$  (like  $\nu_{01}$ ).

Non-axisymmetric tidally aligned modes have small amplitudes near orbital phases 0 and 0.5 due to geometric cancellation. Instead, their amplitudes typically peak near orbital phases 0.25 and 0.75. Modes dominated by  $m = -1$  and  $\ell = 1$  will have phase shifts of  $\sim \pi$  between these two maxima (like the observed mode  $\nu_{06}$ ), while modes dominated by  $m = -2$  and  $\ell = 2$  will have phase shifts of  $\approx 0$ . (like the observed mode  $\nu_{03}$ ). Our models find modes with similar variations in amplitude and phase (right two panels of Figure 5), allowing for tentative mode identifications. Other modes like  $\nu_{22}$  (which peaks near orbital phases 0.125, 0.375, 0.625, and 0.875) can be ascribed to modes dominated by tidally aligned  $m = -1$ ,  $\ell = 2$  modes. Table 1 lists tentative mode assignments for each observed mode, based on the amplitude/frequency modulation described above.

A tentative finding of our pulsation analysis is that the sdB star must be near or past the end of core helium burning. Here, we have identified 14 separate  $m = 0$  modes in the frequency range 260-300  $\text{d}^{-1}$ , whereas only about three acoustic modes (the axisymmetric  $n = 1$  or  $n = 2$  modes for  $\ell = 0, 1, 2$ ) would be expected. However, models near or just past the end of core helium burning contain many g modes in the observed frequency range, which may explain the large number of observable  $m = 0$  modes in such a small frequency range. This conclusion is also supported by the modes  $\nu_{14} = 151.2 \text{ d}^{-1}$ ,  $\nu_{08} = 190.8 \text{ d}^{-1}$ ,  $\nu_{03} = 296.5 \text{ d}^{-1}$ ,  $\nu_{10} = 394.2 \text{ d}^{-1}$ , all of which have amplitude/phase variations consistent with  $\ell = 2$ ,  $m = -2$  modes. The lowest frequency modes  $\nu_{14}$  and  $\nu_{08}$  have frequencies too small to be acoustic modes, and must be predominantly g modes. Assuming they are dominated by  $\ell = 2$  components, only evolved sdB models have a g mode frequency spectrum dense enough to produce those modes, further favoring models that place the sdB star near the point of helium depletion.

One issue with our models is that none of the pulsations are predicted to be excited, which is a problem common to many types of pulsators. It is possible that radiative levitation, which was not included in our models, increases iron group element abundances near the mode excitation region, a key feature for exciting low-order acoustic modes in blue large-amplitude pulsators (BLAPs; Byrne & Jeffery 2020), which have nearly the same temperatures and surface gravities as HD 265435. A detailed asteroseismic analysis of these pulsations and their excitation requires a separate investigation.

We conclude by emphasizing that most of our mode identifications are enabled by the tidal tilting phenomenon, which causes phase and amplitude variation that allows us to determine the dominant  $\ell$  and  $m$  components of the modes. These mode identifications, in

turn, allow for more detailed asteroseismic analyses than would be possible without the tidal tilting phenomenon.

## 5. SUMMARY AND CONCLUSIONS

In this work, we have found that the rich pulsation spectrum of the sdB-white dwarf binary HD 265435 (TIC 68495594) contains 27 frequency multiplets between 160 – 400  $\text{d}^{-1}$  that are split by the orbital frequency ( $\nu_{\text{orb}} = 14.5 \text{ d}^{-1}$ ). We have conclusively shown that these multiplet splittings are due to the fact that the sdB star’s pulsation axis has been tidally tilted into the orbital plane and is roughly aligned with the binary’s tidal axis. Throughout one orbital cycle, the observer views the sdB star over a wide range of latitudinal angles with respect to the tidal axis, causing apparent periodic amplitude and phase shifts of the pulsations with the orbital phase. These shifts in the pulsations’ amplitude and phase yield the observed multiplet splittings.

These amplitude and phase shifts enable us to directly infer the nature of the observed pulsation modes, in many cases enabling us to determine the dominant  $\ell$  and  $|m|$  component of the mode. In turn, this has led us to a more robust understanding of this star’s evolutionary state, finding it is likely near or just past the end of core helium burning. Finally, we have also demonstrated that tidal tilting is possible in both highly evolved stars whose whole envelope has been stripped, as well as in very compact binaries, such as those with  $P_{\text{orb}} \lesssim 100$  minutes. This should further motivate the search for tidally tilted pulsations in a wider range of binaries.

The TESS data promise to be a continuing source of such discoveries as the satellite continues to survey the sky. Moreover, the combination of upcoming and archival data from prior sectors will be beneficial in determining both orbital and pulsational frequencies more precisely. Finally, the 200-s full-frame image cadence in the upcoming Extended Mission 2 (which will enable us to probe up to a Nyquist limit of 216  $\text{d}^{-1}$ , corresponding to a period of just over 6.5 min) will enable us to discover even more tidally tilted pulsators without the need to request targeted observations at a shorter cadence.

## ACKNOWLEDGMENTS

G. H. acknowledges support by the Polish NCN grant 2015/18/A/ST9/00578.

This paper includes data collected by the TESS mission. Funding for the TESS mission is provided by the NASA Science Mission Directorate. Resources supporting this work were provided by the NASA High-End Computing (HEC) Program through the NASA Advanced Supercomputing (NAS) Division at Ames Research Center to produce the SPOC data products.

540 *Facilities*: TESS

541 *Software*: SPOC (Jenkins et al. 2016), *astropy* (As-

542 *trophy* Collaboration et al. 2013, 2018), *numpy* (Harris

543 et al. 2020), *matplotlib* (Hunter 2007), *scipy* (Virtanen et al. 2020), *pandas* (pandas development team 2020; Wes McKinney 2010), PERIOD04 (Lenz & Breger 2005), MESA (Paxton et al. 2011, 2013, 2015, 2018, 2019), GYRE (Townsend & Teitler 2013; Goldstein & Townsend 2020)

## REFERENCES

- 548 Astropy Collaboration, Robitaille, T. P., Tollerud, E. J.,  
549 et al. 2013, *A&A*, 558, A33,  
550 doi: [10.1051/0004-6361/201322068](https://doi.org/10.1051/0004-6361/201322068)
- 551 Astropy Collaboration, Price-Whelan, A. M., Sipőcz, B. M.,  
552 et al. 2018, *AJ*, 156, 123, doi: [10.3847/1538-3881/aabc4f](https://doi.org/10.3847/1538-3881/aabc4f)
- 553 Bowman, D. M., Johnston, C., Tkachenko, A., et al. 2019,  
554 *ApJL*, 883, L26, doi: [10.3847/2041-8213/ab3fb2](https://doi.org/10.3847/2041-8213/ab3fb2)
- 555 Byrne, C. M., & Jeffery, C. S. 2020, *MNRAS*, 492, 232,  
556 doi: [10.1093/mnras/stz3486](https://doi.org/10.1093/mnras/stz3486)
- 557 Charpinet, S., Fontaine, G., Brassard, P., & Dorman, B.  
558 2000, *ApJS*, 131, 223, doi: [10.1086/317359](https://doi.org/10.1086/317359)
- 559 Dziembowski, W. 1977, *AcA*, 27, 203
- 560 Fuller, J., Kurtz, D. W., Handler, G., & Rappaport, S.  
561 2020, *MNRAS*, 498, 5730, doi: [10.1093/mnras/staa2376](https://doi.org/10.1093/mnras/staa2376)
- 562 Goldstein, J., & Townsend, R. H. D. 2020, *ApJ*, 899, 116,  
563 doi: [10.3847/1538-4357/aba748](https://doi.org/10.3847/1538-4357/aba748)
- 564 Handler, G., Jayaraman, R., Kurtz, D. W., Fuller, J., &  
565 Rappaport, S. A. 2022, arXiv e-prints, arXiv:2201.01722.  
566 <https://arxiv.org/abs/2201.01722>
- 567 Handler, G., Kurtz, D. W., Rappaport, S. A., et al. 2020,  
568 *Nature Astronomy*, 4, 684,  
569 doi: [10.1038/s41550-020-1035-1](https://doi.org/10.1038/s41550-020-1035-1)
- 570 Harris, C. R., Millman, K. J., van der Walt, S. J., et al.  
571 2020, *Nature*, 585, 357, doi: [10.1038/s41586-020-2649-2](https://doi.org/10.1038/s41586-020-2649-2)
- 572 Heber, U. 2016, *PASP*, 128, 082001,  
573 doi: [10.1088/1538-3873/128/966/082001](https://doi.org/10.1088/1538-3873/128/966/082001)
- 574 Holdsworth, D. L., Østensen, R. H., Smalley, B., & Telting,  
575 J. H. 2017, *MNRAS*, 466, 5020,  
576 doi: [10.1093/mnras/stx077](https://doi.org/10.1093/mnras/stx077)
- 577 Hunter, J. D. 2007, *Computing in Science & Engineering*, 9,  
578 90, doi: [10.1109/MCSE.2007.55](https://doi.org/10.1109/MCSE.2007.55)
- 579 Jenkins, J. M., Twicken, J. D., McCauliff, S., et al. 2016, in  
580 *Proc. SPIE*, Vol. 9913, *Software and Cyberinfrastructure*  
581 *for Astronomy IV*, 99133E, doi: [10.1117/12.2233418](https://doi.org/10.1117/12.2233418)
- 582 Kilkenny, D., Koen, C., O’Donoghue, D., & Stobie, R. S.  
583 1997, *MNRAS*, 285, 640, doi: [10.1093/mnras/285.3.640](https://doi.org/10.1093/mnras/285.3.640)
- 584 Kurtz, D. W. 1985, *MNRAS*, 213, 773,  
585 doi: [10.1093/mnras/213.4.773](https://doi.org/10.1093/mnras/213.4.773)
- 586 Kurtz, D. W., Kanaan, A., Martinez, P., & Tripe, P. 1992,  
587 *MNRAS*, 255, 289, doi: [10.1093/mnras/255.2.289](https://doi.org/10.1093/mnras/255.2.289)
- 588 Kurtz, D. W., Handler, G., Rappaport, S. A., et al. 2020,  
589 *MNRAS*, 494, 5118, doi: [10.1093/mnras/staa989](https://doi.org/10.1093/mnras/staa989)
- 590 Lenz, P., & Breger, M. 2005, *Communications in*  
591 *Asteroseismology*, 146, 53, doi: [10.1553/cia146s53](https://doi.org/10.1553/cia146s53)
- 592 Lynas-Gray, A. E. 2021, *Frontiers in Astronomy and Space*  
593 *Sciences*, 8, 19, doi: [10.3389/fspas.2021.576623](https://doi.org/10.3389/fspas.2021.576623)
- 594 Montgomery, M. H., & O’Donoghue, D. 1999, *Delta Scuti*  
595 *Star Newsletter*, 13, 28
- 596 pandas development team, T. 2020, *pandas-dev/pandas*:  
597 *Pandas, latest*, Zenodo, doi: [10.5281/zenodo.3509134](https://doi.org/10.5281/zenodo.3509134)
- 598 Paxton, B., Bildsten, L., Dotter, A., et al. 2011, *ApJS*, 192,  
599 3, doi: [10.1088/0067-0049/192/1/3](https://doi.org/10.1088/0067-0049/192/1/3)
- 600 Paxton, B., Cantiello, M., Arras, P., et al. 2013, *ApJS*, 208,  
601 4, doi: [10.1088/0067-0049/208/1/4](https://doi.org/10.1088/0067-0049/208/1/4)
- 602 Paxton, B., Marchant, P., Schwab, J., et al. 2015, *ApJS*,  
603 220, 15, doi: [10.1088/0067-0049/220/1/15](https://doi.org/10.1088/0067-0049/220/1/15)
- 604 Paxton, B., Schwab, J., Bauer, E. B., et al. 2018, *ApJS*,  
605 234, 34, doi: [10.3847/1538-4365/aaa5a8](https://doi.org/10.3847/1538-4365/aaa5a8)
- 606 Paxton, B., Smolec, R., Gaultschy, A., et al. 2019, arXiv  
607 e-prints. <https://arxiv.org/abs/1903.01426>
- 608 Pelisoli, I., Neunteufel, P., Geier, S., et al. 2021, *Nature*  
609 *Astronomy*, 5, 1052, doi: [10.1038/s41550-021-01413-0](https://doi.org/10.1038/s41550-021-01413-0)
- 610 Rappaport, S. A., Kurtz, D. W., Handler, G., et al. 2021,  
611 *MNRAS*, 503, 254, doi: [10.1093/mnras/stab336](https://doi.org/10.1093/mnras/stab336)
- 612 Ricker, G. R., Winn, J. N., Vanderspek, R., et al. 2015,  
613 *Journal of Astronomical Telescopes, Instruments, and*  
614 *Systems*, 1, 014003, doi: [10.1117/1.JATIS.1.1.014003](https://doi.org/10.1117/1.JATIS.1.1.014003)
- 615 Savitzky, A., & Golay, M. J. E. 1964, *Analytical*  
616 *Chemistry*, 36, 1627
- 617 Shibahashi, H., & Kurtz, D. W. 2012, *MNRAS*, 422, 738,  
618 doi: [10.1111/j.1365-2966.2012.20654.x](https://doi.org/10.1111/j.1365-2966.2012.20654.x)
- 619 Townsend, R. H. D., & Teitler, S. A. 2013, *MNRAS*, 435,  
620 3406, doi: [10.1093/mnras/stt1533](https://doi.org/10.1093/mnras/stt1533)
- 621 Van Reeth, T., Southworth, J., Van Beeck, J., & Bowman,  
622 D. M. 2022, arXiv e-prints, arXiv:2201.05359.  
623 <https://arxiv.org/abs/2201.05359>
- 624 Virtanen, P., Gommers, R., Oliphant, T. E., et al. 2020,  
625 *Nature Methods*, 17, 261, doi: [10.1038/s41592-019-0686-2](https://doi.org/10.1038/s41592-019-0686-2)
- 626 Wes McKinney. 2010, in *Proceedings of the 9th Python in*  
627 *Science Conference*, ed. Stéfan van der Walt & Jarrod  
628 Millman, 56 – 61, doi: [10.25080/Majora-92bf1922-00a](https://doi.org/10.25080/Majora-92bf1922-00a)

## APPENDIX

629

**Table 1.** Multifrequency solution for the TESS 20-s cadence photometry of HD 265435. Error estimates for the independent frequencies and pulsation phases at  $T_0$  are given in parentheses in units of the last two significant digits; the errors on the amplitudes are  $\pm 0.05$  mmag. Modes marked as “Unclear” do not have enough information to make a conclusive determination as to their  $\ell$  and  $m$  values.

ID	Freq. ( $\text{d}^{-1}$ )	Ampl. (mmag)	Phase (rad)	Dominant $\ell$ and $m$
$\nu_{01}-6\nu_{orb}$	189.6155(23)	0.22	0.40(21)	
$\nu_{01}-4\nu_{orb}$	218.6775(28)	0.18	2.92(26)	
$\nu_{01}-2\nu_{orb}$	247.7394(06)	0.83	-0.09(06)	
$\nu_{01}-\nu_{orb}$	262.2704(02)	2.74	3.00(02)	
$\nu_{01}$	276.8014(03)	1.82	-0.18(03)	$\ell = 1, m = 0$
$\nu_{01}+\nu_{orb}$	291.3324(02)	3.17	3.02(01)	
$\nu_{01}+2\nu_{orb}$	305.8634(04)	1.19	-0.01(04)	
$\nu_{01}+4\nu_{orb}$	334.9253(14)	0.36	-2.95(13)	
$\nu_{02}-4\nu_{orb}$	205.9939(23)	0.23	-0.47(21)	
$\nu_{02}-2\nu_{orb}$	235.0559(06)	0.91	2.47(05)	
$\nu_{02}-\nu_{orb}$	249.5869(04)	1.43	2.42(03)	
$\nu_{02}$	264.1179(03)	1.98	2.32(02)	$\ell = 2, m = 0$
$\nu_{02}+\nu_{orb}$	278.6488(03)	1.74	2.40(03)	
$\nu_{02}+2\nu_{orb}$	293.1798(04)	1.29	2.50(04)	
$\nu_{02}+4\nu_{orb}$	322.2418(14)	0.38	-0.47(13)	
$\nu_{02}+6\nu_{orb}$	351.3038(21)	0.25	2.67(19)	
$\nu_{03}-4\nu_{orb}$	238.3809(18)	0.29	0.21(17)	
$\nu_{03}-2\nu_{orb}$	267.4429(04)	1.17	0.31(04)	
$\nu_{03}-\nu_{orb}$	281.9739(12)	0.45	-3.14(11)	
$\nu_{03}$	296.5049(03)	1.64	-3.11(03)	$\ell = 2,  m  = 2$
$\nu_{03}+\nu_{orb}$	311.0359(13)	0.39	0.14(12)	
$\nu_{03}+2\nu_{orb}$	325.5668(07)	0.77	0.27(06)	
$\nu_{04}-4\nu_{orb}$	209.2949(15)	0.34	0.77(14)	
$\nu_{04}-2\nu_{orb}$	238.3569(08)	0.68	-2.00(07)	
$\nu_{04}-\nu_{orb}$	252.8879(05)	1.01	-2.14(05)	
$\nu_{04}$	267.4189(04)	1.31	-2.19(04)	$\ell = 2, m = 0$
$\nu_{04}+\nu_{orb}$	281.9498(06)	0.88	-2.23(05)	
$\nu_{04}+2\nu_{orb}$	296.4808(07)	0.7	-2.05(07)	
$\nu_{05}-4\nu_{orb}$	228.1098(14)	0.37	-2.68(13)	
$\nu_{05}-2\nu_{orb}$	257.1718(13)	0.41	0.16(11)	
$\nu_{05}-\nu_{orb}$	271.7027(07)	0.75	-3.01(06)	
$\nu_{05}$	286.2337(09)	0.56	-3.03(08)	$\ell = 2, m = 0$
$\nu_{05}+\nu_{orb}$	300.7647(13)	0.41	0.09(12)	
$\nu_{05}+2\nu_{orb}$	315.2957(09)	0.57	-2.88(08)	

**Table 1** continued

**Table 1** (*continued*)

ID	Freq. (d <sup>-1</sup> )	Ampl. (mmag)	Phase (rad)	Dominant $\ell$ and $m$
$\nu_{06}-2\nu_{orb}$	262.2327(24)	0.21	0.38(22)	
$\nu_{06}-\nu_{orb}$	276.7637(08)	0.65	-2.68(07)	
$\nu_{06}$	291.2947(10)	0.51	0.20(09)	$\ell = 1,  m  = 1$
$\nu_{06}+\nu_{orb}$	305.8256(12)	0.44	0.56(11)	
$\nu_{06}+4\nu_{orb}$	349.4186(26)	0.2	0.95(23)	
$\nu_{07}-2\nu_{orb}$	248.5255(10)	0.53	0.34(09)	
$\nu_{07}-\nu_{orb}$	263.0565(23)	0.23	-2.99(21)	
$\nu_{07}$	277.5874(05)	1.15	0.17(04)	$\ell = 0, m = 0$
$\nu_{07}+\nu_{orb}$	292.1184(29)	0.18	-3.14(27)	
$\nu_{07}+2\nu_{orb}$	306.6494(23)	0.23	0.80(21)	
$\nu_{07}+4\nu_{orb}$	335.7114(20)	0.25	0.41(19)	
$\nu_{08}-2\nu_{orb}$	161.7450(20)	0.25	-3.09(19)	
$\nu_{08}$	190.8069(14)	0.37	0.32(13)	$\ell = 2,  m  = 2$
$\nu_{08}+2\nu_{orb}$	219.8689(13)	0.39	-2.84(12)	
$\nu_{09}-2\nu_{orb}$	248.9320(09)	0.57	-0.14(08)	
$\nu_{09}-\nu_{orb}$	263.4630(06)	0.87	2.88(05)	
$\nu_{09}$	277.9940(27)	0.19	-0.11(24)	$\ell = 1,  m  = 0$
$\nu_{09}+\nu_{orb}$	292.5249(06)	0.92	3.00(05)	
$\nu_{09}+2\nu_{orb}$	307.0559(25)	0.2	-0.22(23)	
$\nu_{10}-2\nu_{orb}$	365.1796(25)	0.2	2.93(23)	
$\nu_{10}$	394.2416(11)	0.46	0.31(10)	$\ell = 2,  m  = 2$
$\nu_{10}+2\nu_{orb}$	423.3036(13)	0.39	-3.03(12)	
$\nu_{11}-2\nu_{orb}$	234.4928(19)	0.27	-2.82(17)	
$\nu_{11}-\nu_{orb}$	249.0238(13)	0.41	-2.92(12)	
$\nu_{11}$	263.5548(10)	0.49	-3.01(10)	$\ell = 2, m = 0$
$\nu_{11}+\nu_{orb}$	278.0858(10)	0.54	-2.88(09)	
$\nu_{11}+2\nu_{orb}$	292.6167(11)	0.47	-2.56(10)	
$\nu_{12}-3\nu_{orb}$	252.6979(21)	0.25	-0.08(19)	
$\nu_{12}-2\nu_{orb}$	267.2289(18)	0.3	-0.43(16)	
$\nu_{12}-\nu_{orb}$	281.7599(12)	0.45	-0.51(11)	
$\nu_{12}$	296.2908(05)	1.06	2.77(04)	Unclear
$\nu_{13}-2\nu_{orb}$	252.7658(31)	0.17	-1.50(28)	
$\nu_{13}-\nu_{orb}$	267.2968(17)	0.31	1.55(15)	
$\nu_{13}$	281.8278(09)	0.61	-1.90(08)	$\ell = 2, m = 0$
$\nu_{13}+\nu_{orb}$	296.3588(21)	0.25	1.09(19)	
$\nu_{13}+2\nu_{orb}$	310.8897(11)	0.46	-1.59(10)	
$\nu_{14}-2\nu_{orb}$	122.1339(19)	0.27	0.32(18)	
$\nu_{14}$	151.1959(16)	0.33	-2.96(14)	$\ell = 2,  m  = 2$
$\nu_{14}+2\nu_{orb}$	180.2579(26)	0.2	0.24(23)	
$\nu_{15}-2\nu_{orb}$	238.8100(15)	0.34	-1.95(14)	

**Table 1** *continued*

**Table 1** (*continued*)

ID	Freq. (d <sup>-1</sup> )	Ampl. (mmag)	Phase (rad)	Dominant $\ell$ and $m$
$\nu_{15} - \nu_{orb}$	253.3410(12)	0.44	-1.75(11)	
$\nu_{15}$	267.8720(10)	0.5	-2.02(09)	$\ell = 2, m = 0$
$\nu_{15} + \nu_{orb}$	282.4030(20)	0.26	-1.76(18)	
$\nu_{15} + 2\nu_{orb}$	296.9339(17)	0.3	-1.80(16)	
$\nu_{16} - 2\nu_{orb}$	327.5495(25)	0.21	2.16(23)	
$\nu_{16} - \nu_{orb}$	342.0805(16)	0.32	2.27(15)	
$\nu_{16}$	356.6115(04)	1.33	2.90(04)	$\ell = 0, m = 0$
$\nu_{17} - \nu_{orb}$	254.9016(16)	0.33	1.66(14)	
$\nu_{17}$	269.4326(12)	0.43	-1.66(11)	$\ell = 1, m = 0$
$\nu_{17} + \nu_{orb}$	283.9636(12)	0.43	1.32(11)	
$\nu_{18} - 3\nu_{orb}$	256.1142(25)	0.21	0.99(23)	
$\nu_{18} - 2\nu_{orb}$	270.6452(12)	0.44	-2.09(11)	
$\nu_{18}$	299.7071(13)	0.41	1.20(12)	$\ell = 2,  m  = 2$
$\nu_{18} + \nu_{orb}$	314.2381(15)	0.34	-2.06(14)	
$\nu_{19} - 3\nu_{orb}$	273.3898(10)	0.5	-1.75(09)	
$\nu_{19} - 2\nu_{orb}$	287.9207(15)	0.35	1.31(13)	
$\nu_{19} - \nu_{orb}$	302.4517(11)	0.47	-1.64(10)	
$\nu_{19}$	316.9827(06)	0.88	1.61(05)	Unclear
$\nu_{19} + 2\nu_{orb}$	346.0447(23)	0.23	-1.26(21)	
$\nu_{20} - 2\nu_{orb}$	244.9160(17)	0.3	-1.15(16)	
$\nu_{20} - \nu_{orb}$	259.4469(17)	0.31	-1.39(15)	
$\nu_{20}$	273.9779(11)	0.46	-1.46(10)	$\ell = 2, m = 0$
$\nu_{20} + \nu_{orb}$	288.5089(11)	0.45	-1.34(10)	
$\nu_{20} + 2\nu_{orb}$	303.0399(19)	0.27	-1.27(17)	
$\nu_{21} - 3\nu_{orb}$	217.7425(22)	0.23	3.03(20)	
$\nu_{21} - \nu_{orb}$	246.8045(13)	0.41	-0.16(12)	
$\nu_{21}$	261.3355(09)	0.55	-0.29(09)	Unclear
$\nu_{22} - 2\nu_{orb}$	470.2932(17)	0.31	-0.41(15)	
$\nu_{22}$	499.3552(23)	0.22	-0.53(21)	$\ell = 2,  m  = 1$
$\nu_{22} + 2\nu_{orb}$	528.4172(21)	0.25	2.79(19)	
$\nu_{23} - 2\nu_{orb}$	240.8715(24)	0.21	-2.41(22)	
$\nu_{23} - \nu_{orb}$	255.4025(25)	0.21	-2.56(22)	
$\nu_{23}$	269.9335(11)	0.47	-2.43(10)	$\ell = 0, m = 0$
$\nu_{24} - 2\nu_{orb}$	255.2800(30)	0.17	-0.98(27)	
$\nu_{24}$	284.3419(12)	0.44	-1.34(11)	$\ell = 1, m = 0$
$\nu_{25} - \nu_{orb}$	332.5411(29)	0.18	-0.11(26)	
$\nu_{25}$	347.0721(13)	0.39	3.10(12)	$\ell = 0, m = 0$
$\nu_{26} - \nu_{orb}$	232.1108(33)	0.16	-0.39(30)	
$\nu_{26}$	246.6418(08)	0.65	-0.68(07)	$\ell = 0, m = 0$
$\nu_{26} + \nu_{orb}$	261.1727(27)	0.19	-0.77(25)	

**Table 1** *continued*

**Table 1** (*continued*)

ID	Freq. ( $\text{d}^{-1}$ )	Ampl. (mmag)	Phase (rad)	Dominant $\ell$ and $m$
$\nu_{27} - \nu_{orb}$	327.5779(21)	0.25	2.00(19)	
$\nu_{27}$	342.1089(21)	0.25	-1.98(19)	$\ell = 1, m = 0$
$\nu_{27} + \nu_{orb}$	356.6399(13)	0.39	1.65(12)	
$\nu_{28}$	165.5120(23)	0.23	-0.12(21)	Unclear
$\nu_{29}$	371.1332(07)	0.72	2.81(07)	Unclear
$\nu_{30}$	396.5577(15)	0.33	-3.12(14)	Unclear
$\nu_{31}$	373.4229(20)	0.25	-0.20(19)	Unclear
$\nu_{02} + \nu_{04} - \nu_{orb}$	517.0057(18)	0.29	-2.16(16)	
$\nu_{02} + \nu_{04} + \nu_{orb}$	546.0677(19)	0.27	-2.69(18)	
$\nu_{07} + \nu_{09} - \nu_{orb}$	541.0504(19)	0.27	2.51(17)	
$\nu_{07} + \nu_{09} + \nu_{orb}$	570.1124(18)	0.29	-0.94(17)	
$2\nu_{09} + \nu_{orb}$	570.5189(17)	0.3	1.06(16)	
$\nu_{09} + \nu_{21} + \nu_{orb}$	553.8604(15)	0.34	-2.01(14)	
$2\nu_{09} - \nu_{orb}$	541.4569(14)	0.37	-2.19(13)	